theoretically possible increase based on the well-defined properties of RuBisCO (Fig. 3). At 25°C, an increase in [CO_2] to 550 ppm should increase light-saturated photosynthesis by 36%. The average increase observed for C_3 crops in FACE was 20% for the daily integral of photosynthetic CO_2 uptake, 17% for total biomass, and just 13% for yield (Fig. 3). This suggests that a series of feedbacks operate in the field to constrain realization of the potential benefits of elevated [CO_2]. Only with a thorough high-priority R&D effort might we overcome these feedbacks and achieve the potential gains in food supply.

The FACE experiments clearly show that much lower CO_2 fertilization factors should be used in model projections of future yields; however, the present experiments are limited in the range of growing conditions that they cover. Scientists have not investigated the interactive effects of simultaneous change in [CO_2], [O_3], temperature, and soil moisture. Technological advances suggest that large-scale open-air facilities to investigate these interactions over controlled gradients of variation are now possible (*26*). Although we have projected results to 2050, this may be too far in the future to spur commercial R&D, but it must not be seen as too distant to discourage R&D in the public sector, given the long lead times that may be needed to avoid global food shortage.

References and Notes

1. G. Hoogenboom *et al.*, in *Climate Change and Agriculture: Analysis of Potential International Impacts. ASA Special Publication no. 59* (American Society of Agronomy, Madison, WI, 1995), pp. 51–75.
2. M. Parry, C. Rosenzweig, M. Livermore, *Philos. Trans. R. Soc. London Ser. B* **360**, 2125 (2005).
3. R. M. Peart, J. W. Jones, R. B. Curry, K. J. Boote, L. H. Allen, in *The Potential Effects of Global Climate Change on the United States, Appendix C, Report to Congress*, J. B. Smith, D. A. Tirpak, Eds. (EPA-230-05-89-053, U.S. Environmental Protection Agency, Washington, DC, 1989), pp. 2–54.
4. C. O. Stockle, J. R. Williams, N. J. Rosenberg, C. A. Jones, *Agric. Syst.* **38**, 225 (1992).
5. H. Gitay, S. Brown, W. Easterling, B. Jallow, in *Climate Change 2001: Impacts, Adaptation, and Vulnerability*, J. J. McCarthy, O. F. Canziani, N. A. Leary, D. J. Dokken, K. S. White, Eds. (Cambridge Univ. Press, Cambridge, 2001), pp. 237–342.
6. M. Parry, C. Rosenzweig, A. Iglesias, G. Fischer, M. Livermore, *Global Environ. Change* **9**, S51 (1999).
7. M. L. Parry, C. Rosenzweig, A. Iglesias, M. Livermore, G. Fischer, *Global Environ. Change* **14**, 53 (2004).
8. J. T. Houghton *et al.*, Eds., *Climate Change 2001: The Scientific Basis. Contribution of Working Group I to the Third Assessment Report of the Intergovernmental Panel on Climate Change* (Cambridge Univ. Press, Cambridge, 2001).
9. S. P. Long, E. A. Ainsworth, A. Rogers, D. R. Ort, *Annu. Rev. Plant Biol.* **55**, 591 (2004).
10. S. von Caemmerer, R. T. Furbank, *Photosynth. Res.* **77**, 191 (2003).
11. R. M. Adams *et al.*, *Nature* **345**, 219 (1990).
12. C. Rosenzweig, A. Iglesias, in *Understanding Options for Agricultural Production*, G. Y. Tsuji, G. Hoogenboom, P. K. Thornton, Eds. (Kluwer Academic, Dordrecht, Netherlands, 1998), pp. 267–292.
13. R. A. Brown, N. J. Rosenberg, *Clim. Change* **41**, 73 (1999).
14. R. C. Izaurralde, N. J. Rosenberg, R. A. Brown, A. M. Thomson, *Agric. For. Meteorol.* **117**, 97 (2003).
15. A. M. Thomson, R. A. Brown, N. J. Rosenberg, R. C. Izaurralde, V. Benson, *Clim. Change* **69**, 43 (2005).
16. L. H. Allen *et al.*, *Global Biogeochem. Cycles* **1**, 1 (1987).
17. J. D. Cure, B. Acock, *Agric. For. Meteorol.* **38**, 127 (1986).
18. B. A. Kimball, *Agron. J.* **75**, 779 (1983).
19. A. Anand *et al.*, *J. Exp. Bot.* **54**, 1101 (2003).
20. B. Black, *Abstr. Pap. Am. Chem.* **228**, U84 (2004).
21. E. A. Ainsworth *et al.*, *Global Change Biol.* **8**, 695 (2002).
22. D. Whitehead *et al.*, *J. Biogeogr.* **22**, 307 (1995).
23. A. R. McLeod, S. P. Long, *Adv. Ecol. Res.* **28**, 1 (1999).
24. F. Miglietta, M. Lanini, M. Bindi, V. Magliulo, *Global Change Biol.* **3**, 417 (1997).
25. F. W. Lipfert, Y. Alexander, G. R. Hendrey, K. F. Lewin, J. Nagy, *Crit. Rev. Plant Sci.* **11**, 143 (1992).
26. J. Nösberger *et al.*, Eds. *Managed Ecosystems and CO_2 Case Studies, Processes, and Perspectives, Ecological Studies*, vol. 187 (Springer, Berlin, 2006).
27. M. R. Shaw *et al.*, *Science* **298**, 1987 (2002).
28. E. A. Ainsworth, S. P. Long, *New Phytol.* **165**, 351 (2005).
29. A. D. B. Leakey, C. J. Bernacchi, F. G. Dohleman, D. R. Ort, S. P. Long, *Global Change Biol.* **10**, 951 (2004).
30. A. D. B. Leakey *et al.*, *Plant Physiol.* **140**, 779 (2006).
31. G. W. Wall *et al.*, *New Phytol.* **152**, 231 (2001).
32. M. J. Ottman *et al.*, *New Phytol.* **150**, 261 (2001).
33. M. R. Ashmore, in *Air Pollution and Plant Life*, J. N. B. Bell, M. Treshow, Eds. (Wiley, New York, 2002), pp. 89–118.
34. P. B. Morgan, T. A. Mies, G. A. Bollero, R. L. Nelson, S. P. Long, *New Phytol.* **170**, 333 (2006).
35. S. P. Long, E. A. Ainsworth, A. D. B. Leakey, P. B. Morgan, *Philos. Trans. R. Soc. London Ser. B* **360**, 2011 (2005).
36. J. S. Amthor, *Field Crops Res.* **73**, 1 (2001).
37. Materials and methods for meta-analyses are available as supporting material on *Science* Online. Full results from the meta-analyses summarized in Table 1 are presented in table S2 with references in appendix S1. C_4 crop yield responses to elevated [CO_2] are presented in table S3 with references in appendix S2.

38. This work was supported by the Illinois Council for Food and Agricultural Research, Archer Daniels Midland Company, U.S. Department of Agriculture, U.S. Department of Energy (grant DE-FG02-04ER63849), and Illinois Agricultural Experiment Station.

Supporting Online Material

www.sciencemag.org/cgi/content/full/312/5782/1918/DC1
Materials and Methods
Tables S1 to S3
References
Appendices S1 and S2

1 March 2006; accepted 15 May 2006
10.1126/science.1114722

Frictional Afterslip Following the 2005 Nias-Simeulue Earthquake, Sumatra

Ya-Ju Hsu,[1]* Mark Simons,[1] Jean-Philippe Avouac,[1] John Galetzka,[1] Kerry Sieh,[1] Mohamed Chlieh,[1] Danny Natawidjaja,[2] Linette Prawirodirdjo,[3] Yehuda Bock[3]

Continuously recording Global Positioning System stations near the 28 March 2005 rupture of the Sunda megathrust [moment magnitude (M_w) 8.7] show that the earthquake triggered aseismic frictional afterslip on the subduction megathrust, with a major fraction of this slip in the up-dip direction from the main rupture. Eleven months after the main shock, afterslip continues at rates several times the average interseismic rate, resulting in deformation equivalent to at least a M_w 8.2 earthquake. In general, along-strike variations in frictional behavior appear to persist over multiple earthquake cycles. Aftershocks cluster along the boundary between the region of coseismic slip and the up-dip creeping zone. We observe that the cumulative number of aftershocks increases linearly with postseismic displacements; this finding suggests that the temporal evolution of aftershocks is governed by afterslip.

Slip on faults occurs as a combination of relatively continuous aseismic creep and transient slip events. These transient events occur as earthquakes radiating seismic waves, and also as aseismic events with characteristic time scales of days to years. A better understanding of the physical factors that control the relative amounts and location of seismic and aseismic slip is a key goal in the study of fault mechanics and in particular can affect assessments of regional seismic and tsunami hazards. After a large earthquake, postseismic deformation may result from earthquake-induced slip along the plate interface, commonly referred to as afterslip, and as viscoelastic relaxation in the volume surrounding the fault rupture (*1*–*3*). Thus, well-positioned postseismic observations can probe the mechanical properties of subduction megathrusts and the media that surround them.

Geodetic and seismological investigations suggest that typical subduction megathrust earthquakes involve fault rupture at depths between ~10 km and ~50 km, and that rupture all the way up to the trench is rare (*4*). However, evidence for slip on the shallowest portions of a megathrust has been notoriously difficult to evaluate. We commonly assume that seismic slip decreases in both up-dip and down-dip directions, presumably bounded by regions where frictional behavior of the fault does not support stick-slip (i.e., seismic) rupture (*5*).

[1]Division of Geological and Planetary Sciences, California Institute of Technology, Pasadena, CA 91125, USA. [2]Research Center for Geotechnology, Indonesian Institute of Sciences, Bandung 40135, Indonesia. [3]Institute of Geophysics and Planetary Physics, University of California, San Diego, La Jolla, CA 92093, USA.

*To whom correspondence should be addressed. E-mail: yaru@gps.caltech.edu

These variations with depth are thought to result from the direct effect of temperature on the rheology of the plate interface or from indirect effects associated with metamorphism (*6*–*8*). In particular, the frictional behavior of the shallowest part of the megathrust is commonly assumed to be governed by clay minerals that promote rate-strengthening friction (*6*). Down-dip of the seismogenic zone, the megathrust presumably creeps continuously at approximately the plate convergence rate. In contrast to down-dip variations in seismogenic behavior, the underlying causes for along-strike variations remain enigmatic (*9*–*13*). Furthermore, what is actually happening along the shallowest portion of the megathrust is poorly known because of a lack of proximal geodetic observations in most areas. In contrast to most seismically active subduction zones, the presence of islands relatively close to the trench and above the seismogenic portions of the Sunda megathrust makes it possible to constrain coseismic, postseismic, and interseismic processes from geodetic monitoring and paleogeodetic studies (Fig. 1).

The 28 March 2005 M_w 8.7 Nias-Simeulue earthquake resulted from rupture of the subduction megathrust off the shore of northwestern Sumatra, southeast of the 26 December 2004 M_w 9.1 Aceh-Andaman rupture (*14*, *15*). In this region, the Indo-Australian plate converges obliquely toward the Sunda Block at a rate of ~57 mm/year (*16*) (Fig. 1, inset). This convergence is approximately partitioned into a 40 mm/year trench-normal component on the megathrust and a 25 mm/year component of dextral slip along the Sumatran Fault (*17*, *18*). The subduction megathrust off the shore of Sumatra has produced four earthquakes with magnitudes larger than 8 since 1797, including a M ~8.5 event near Nias in 1861 (*19*, *20*) that occurred in the approximate region of the southern asperity of the 2005 event. Paleogeodetic and recent continuous Global Positioning System (cGPS) data from the Sumatran GPS Array (SuGAr) (*21*) as well as survey-mode GPS data suggest that the shallow portion of the megathrust up-dip of the Batu Islands (Fig. 1) is creeping during the interseismic period (*19*, *22*). The 2005 rupture occurred beneath the northern portion of SuGAr, permitting a record of both coseismic and postseismic deformation.

The coseismic and postseismic slip model. We use cGPS data spanning the first 11 months after the 2005 Nias-Simeulue earthquake, including nine SuGAr sites and the station SAMP, installed by the Indonesian National Surveying Agency (BAKOSURTANAL) (Fig. 1) (*15*, *23*). Three sites (LEWK, BSIM, and LHWA) were installed about a month before the Nias-Simeulue earthquake; three sites (PBLI, BITI, and BTHL) were installed 5 months after the earthquake; and three sites (PSMK, PTLO, and PBAI) just south of the Equator were installed in mid-2002, well before the Aceh-Andaman earthquake. In addition, 102 field measurements of vertical displacements from coral microatolls constrain the coseismic slip model. In the modeling of postseismic deformation, we use only the cGPS data.

The models considered here assume that all surface deformation is caused by slip on a dip-

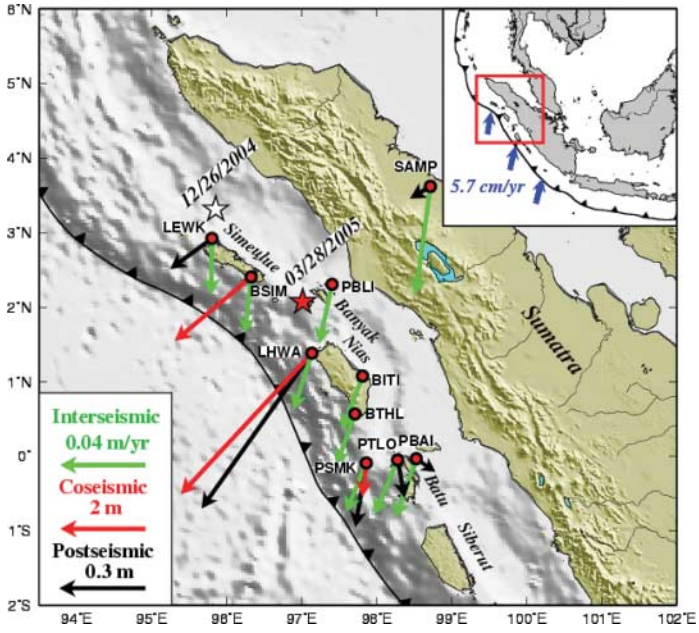

Fig. 1. Surface displacement estimated at the location of the cGPS stations in northern Sumatra for three time periods: The interseismic period before the 2004 Aceh-Andaman earthquake (green arrows), the 2005 Nias-Simeulue earthquake coseismic period (red arrows), and the 11-month period after the 2005 earthquake (black arrows). White and red stars indicate epicenters of 2004 Aceh-Andaman and 2005 Nias-Simeulue earthquakes, respectively. The black barbed line denotes the Sunda megathrust. Interseismic displacements for LEWK, BSIM, and LHWA are not derived from cGPS data, but rather from a model constrained by campaign GPS data (*46*). Estimates of coseismic displacement for PTLO and PBAI are too small to be visible at this scale. Three sites (PBLI, BITI, and BTHL) were installed after the earthquake and do not have estimates of coseismic displacements. (**Inset**) Regional geography with motion of the Australian plate relative to the Sunda Block indicated by blue arrows.

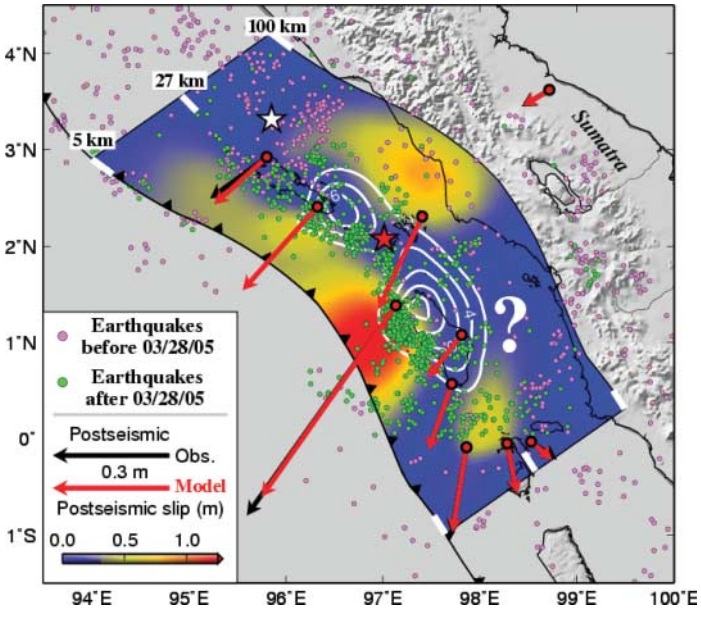

Fig. 2. Compilation of inferred coseismic and postseismic slip, illustrating extensive afterslip up-dip from the main shock and a lack of substantial overlap between seismogenic and aseismic regions. Distribution of coseismic slip is indicated by white contours at intervals of 2 m; color indicates cumulative postseismic slip during the 9 months after the main shock. Black and red vectors indicate observed and predicted GPS observations, respectively. Displacements measured at the stations deployed 5 months after the main shock are not shown. White and red stars are epicenters of 2004 Aceh-Andaman and 2005 Nias-Simeulue earthquakes, respectively. Pink and green dots denote earthquakes with m_b > 4.5 before (*24*) and after (*43*) the 2005 event. The regions of high seismicity correspond to the transition between regions of coseismic and aseismic slip. The large question mark east of Nias indicates the region where afterslip may have occurred but is not detectable by the existing cGPS network. White tick marks on the northern and southern boundaries of the postseismic slip model indicate depths along the megathrust.

ping fault plane (i.e., the megathrust) embedded in a horizontally layered elastic space (*23*). The fault geometry differs slightly from that used previously (*24*); it is extended in length and width and has an additional segment at depth. The model fault approximately follows the curvature of the trench and changes dip from 10° to 30° at a depth of 27 km. The bottom of the model fault occurs at 100 km depth (Fig. 2) and follows the Wadati-Benioff zone, as defined by relocated seismicity spanning the period 1964 to 2005 (*25*). Constraints on the dip angle of the shallower portion come from the joint analysis of coseismic geodetic and seismic data (*26*), which yields a preferred dip angle for the seismogenic fault of between 8° and 12°. This range of dips can account simultaneously for the geodetic displacements, the seismic moment, and the amplitude of the spheroidal and toroidal normal modes (*26*).

We invert both coseismic and postseismic slip distributions with the use of the same fault geometry and a priori constraints on the rake (*23*). We have explored the impact of minimizing model roughness and model length (figs. S1 and S2). The time-dependent inversion of postseismic slip history adopts the extended network inversion filter (ENIF) approach (*27*, *28*). The GPS time series and model predictions, excluding estimates of benchmark wobble and reference-frame errors, are shown in fig. S3 (*29*).

The coseismic slip distribution, constrained by both the cGPS and the coral microatoll data (*24*), has two major loci of slip, separated by a region of negligible slip near the hypocenter (Fig. 2). Thus, the Nias-Simeulue earthquake resulted from two distinct ruptures: a M_w 8.2 event to the north of the hypocenter and a M_w 8.5 event to the south. Within the limits of resolution, the peak model slip values are 8 m (in the north) and 11 m (in the south). This coseismic model is similar to an earlier version that was determined using a slightly different megathrust geometry (*24*). Our present approach to damping is more rigorous and leads to a more spatially compact distribution of slip (*23*). The spatial coverage of data enables discrimination of the spatial extent of primary slip areas (fig. S1). The lack of up-dip coseismic slip is a robust feature of our model.

The postseismic slip distribution results from inversion of only the cGPS data. Even without microatoll data, resolution tests suggest that we can resolve up-dip afterslip well, whereas we can resolve down-dip afterslip only north of the hypocenter (fig. S2). The spatial distribution of postseismic slip remains basically stationary throughout the entire 11-month period (figs. S5 and S6). We note that the availability of data from three additional sites (PBLI, BITI, and BTHL) south of the rupture increases the model spatial resolution for later periods (fig. S6). Given that the pattern of slip is constant when we do not use these sites, we infer that the pattern we estimate including these sites is likely to be representative of the earlier period as well (fig. S6).

Afterslip occurs in three primary regions: up-dip, down-dip, and south of the coseismic rupture (Fig. 2). The most extensive resolvable region of afterslip lies up-dip of the coseismic rupture, where the maximum amount of afterslip over 11 months is ~1.4 m. Our confidence in the relative location of coseismic and postseismic slip is primarily driven by the observations of vertical displacements at two cGPS sites, LHWA and BSIM. These sites show coseismic uplift of 2.88 m and 1.60 m, respectively, but postseismic subsidence of 0.17 m and 0.05 m.

In the first 11 months after the earthquake, cumulative fault slip of ~0.5 m occurs both beneath the Batu Islands and down-dip of the coseismic rupture. The extent of down-dip slip is only loosely constrained because only one cGPS site, SAMP, provides data from mainland Sumatra. Indeed, there may have been considerable afterslip east of Nias, but we do not have sufficient data to resolve it. In many portions of the fault, the slip rate after 11 months is still about twice the long-term average plate convergence rate.

Discussion. The good fits to both vertical and horizontal components of coseismic and postseismic displacements suggest that our assumed fault geometry is adequate and that both coseismic and postseismic deformation resulted from slip on the megathrust. In the first 11 months of postseismic deformation, we see no evidence indicative of viscoelastic relaxation. This is probably due to the proximity of the geodetic stations to the rupture and to the short time span of the observations. Afterslip in the 11 months following the main shock has a geodetic moment of at least 2.5×10^{21} N·m, equivalent to an M_w 8.2 event or at least 25% of the coseismic moment. The estimate of postseismic geodetic moment is a minimum estimate, because there are likely to be regions of afterslip not resolved with the available data.

Most of the coseismic slip occurred within 150 km of the trench and within the locked fault zone, as inferred from modeling of paleogeodetic and geodetic data (*19*, *22*, *30*, *31*). To first order, and within the inherent limits of our model resolution, the region with afterslip surrounds the area that slipped during the earthquake. There appears to be little overlap between the coseismic and aseismic patches. Bearing in mind the limitations in spatial resolution, we find that 95% of the coseismic potency was released at depths between 13 and 48 km during the 2005 event, with a maximum at ~22 km (fig. S7).

Generally speaking, the inferred rakes of both coseismic and postseismic slip are parallel to each other, approximately perpendicular to the trench, and consistent with previous inferences of strain partitioning across the forearc (*32*, *33*). An exception to this behavior occurs

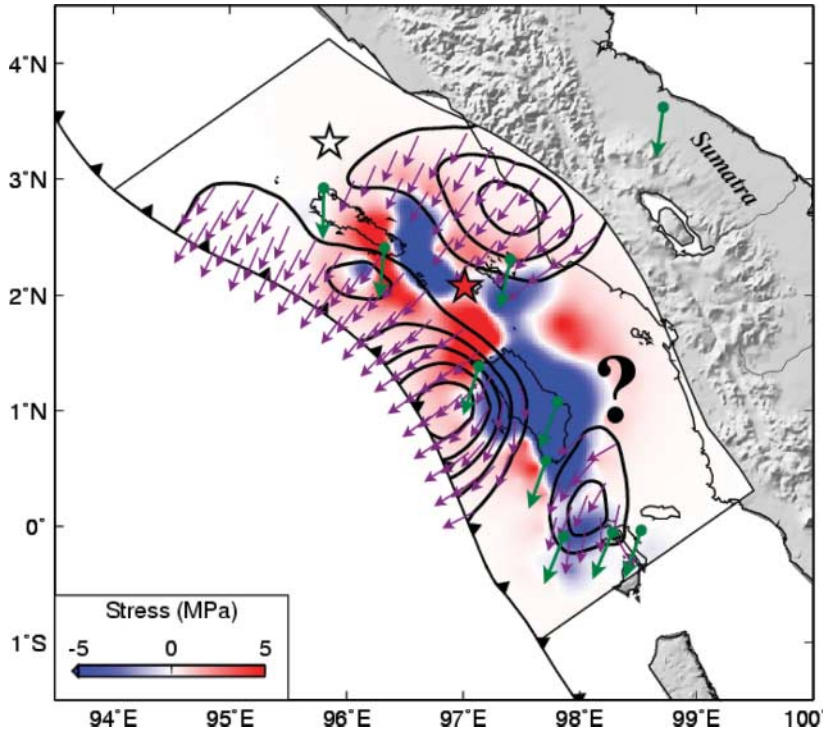

Fig. 3. Coulomb stress change Δ*CFS* (color) on the plate interface and amplitude of postseismic slip (black contours at 0.25-m intervals). For clarity, the model of coseismic slip (Fig. 2) is spatially smoothed before contouring. Purple arrows indicate the rake of the afterslip; green arrows indicate the rake of the interseismic velocity modeled/observed at the surface. White and red stars are epicenters of 2004 Aceh-Andaman and 2005 Nias-Simeulue earthquakes, respectively. The question mark east of Nias indicates a region where our afterslip model is not well constrained because of poor data coverage.

in the south, near the Batu Islands, where the coseismic and postseismic models predict slip rakes that are parallel to the general direction of convergence between the Australian plate and the Sunda Block (Fig. 3). Although poorly constrained, such behavior implies along-strike variations in strain partitioning.

The correlation between coseismic Coulomb stress change, ΔCFS, on the plate interface and the distribution of afterslip (Fig. 3) (*23*) suggests that afterslip is a response of the megathrust to the sudden increase of stress due to the earthquake rupture. The patch with large afterslip up-dip of the coseismic rupture clearly coincides with a zone of increased ΔCFS; this correlation also seems to hold for the down-dip afterslip zone, except east of Nias where the afterslip model is poorly resolved.

The coseismic slip distribution (Fig. 2) shows a distinct saddle between the Simeulue and Nias patches. This region of low slip corresponds to the location of the hypocenter and to the location of a distinct north-south bend in the band of aftershocks (Fig. 2). Previous studies have suggested that a structural tear occurs in this region, corresponding to the Batee Fault, and may be associated with more complex megathrust geometry than that used here (*17*, *34*).

To test the extent to which the spatial variations in slip are stationary in time, we consider historical and paleogeodetic records (*19*, *20*). Southeast of Nias, beneath the Batu Islands, the region of 2005 afterslip correlates with a prominent cluster of medium-sized earthquakes in the past century (*20*). However, coral microatolls show that, as in 2005, vertical deformation during the great historical earthquakes of 1797, 1833, and 1861 was small (*35*). Hence, we presume that megathrust slip in this region is primarily aseismic, with the medium-sized earthquakes representing small, spatially limited locked regions (*22*). We have inferred similarly low seismogenic coupling beneath the northern half of Simeulue in the region separating the 2004 and 2005 events (*24*). Seismicity preceding the 2005 earthquake (*25*) reveals distinct northeast-southwest–trending zones near northeastern Simeulue and near the Batu Islands (Fig. 2). We suggest that these zones that experience frequent small earthquakes during the interseismic period are likely to be regions dominated by aseismic slip. Because of the higher rates of seismicity in these regions, it may be more likely that a large megathrust event would nucleate there and eventually grow into areas that are more tightly coupled. Such behavior may be seen for the Nias-Simeulue earthquake as well as the 2004 Aceh-Andaman and 1995 Antofagasta, Chile, earthquakes (*12*, *15*).

The cGPS postseismic displacement histories are well fit if we assume that afterslip results from rate-strengthening frictional sliding of the plate interface in response to the coseismic stress change (Fig. 4, A to C) (*23*). The model is a system consisting of a spring and a slider with a single degree of freedom (*36*), where the slider obeys an experimental rate-strengthening friction law (*37*, *38*): $\tau_{ss} = \sigma_n\mu^* + A\sigma_n \ln(V/V^*)$, where τ_{ss} is the driving shear stress, σ_n is the normal stress, A is a positive rheological parameter, V is the sliding velocity, and μ^* and V^* are reference values. The postseismic displacement follows the predicted $\log[1 + (t/T_{GPS})]$ temporal evolution, where the characteristic time, T_{GPS}, is estimated to be ~3 days, and $d\tau_{ss}/d \ln V = A\sigma_n$ is on the order of 0.2 to 0.7 MPa. Alternatively, by analyzing the evolution of slip as a function of the evolving postseismic stresses according to our afterslip model (*39*), we find $A\sigma_n$ to be ~0.2 MPa both up-dip and down-dip of the coseismic rupture (fig. S8). If we assume that hydrostatic ambient pore pressure gives values of effective normal stress due to overburden of ~200 MPa and ~1000 MPa for the up-dip (~10 km) and down-dip regions (~60 km), respectively, these values result in estimates of A of $\sim 5 \times 10^{-4}$, comparable to the value of $\sim 10 \times 10^{-4}$ at 35 km depth derived from afterslip following the 2003 M_w 8.0 Tokachi-oki, Japan, earthquake (*39*), or the value of 3×10^{-4} at 50 km depth for the 2001 M_w 8.4 Arequipa, Peru, earthquake (*40*). These values are one to two orders of magnitude lower than estimated in laboratory studies (*41*, *42*). A value of A at the lower end of experimental estimates ($\sim 50 \times 10^{-4}$) would imply a low effective normal stress of ~40 MPa. Any explanation for such a low value is conjectural; high pore pressure is one possibility.

About 2100 aftershocks with body wave magnitude $m_b > 3$ (*43*) occurred in the first year following the 2005 event. These aftershocks amount to only ~7% of the postseismic geodetic moment, indicating that afterslip was essentially aseismic. Most of these aftershocks form a distinct

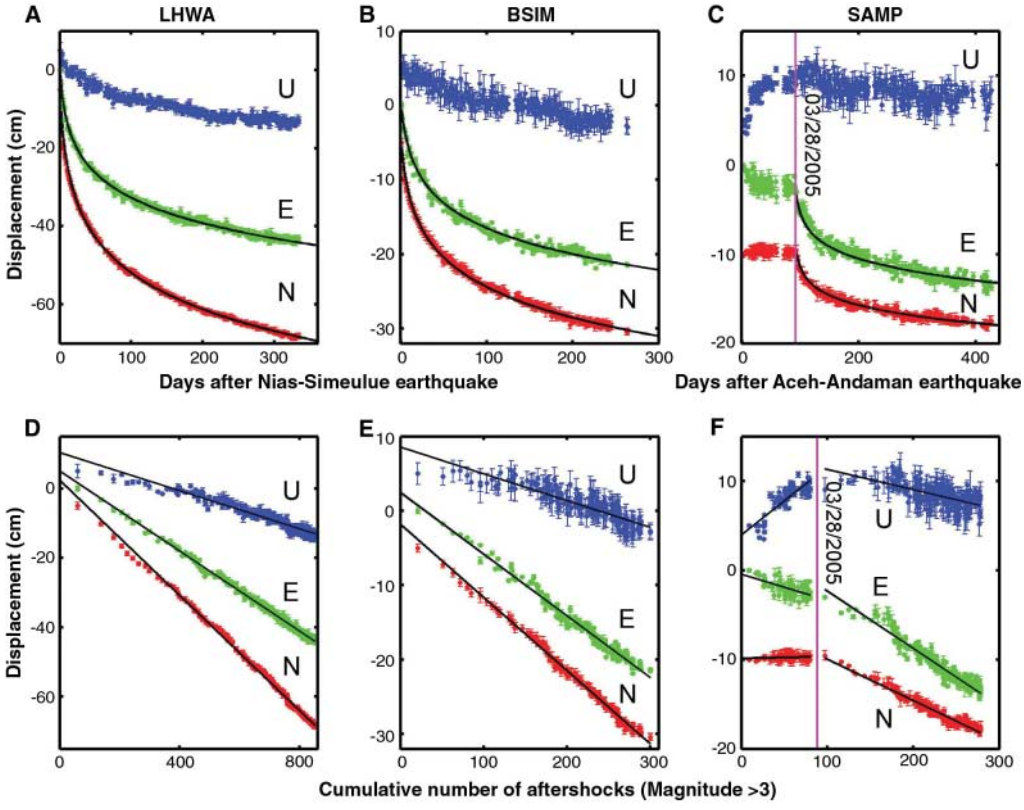

Fig. 4. Observed and modeled postseismic displacements (**A** to **C**) and the relationship of these displacements to the cumulative number of aftershocks near each of the stations (**D** to **F**). Black solid lines in (A) to (C) are estimated from a one-dimensional spring-slider model in which afterslip obeys a velocity-strengthening friction law [see (*23*) for analytical functions and model parameters] (*44*). Blue, green, and red refer to vertical (U), east (E), and north (N) displacements, respectively. Note that the scale differs between panels. Regions used to calculate cumulative seismicity are shown in fig. S10.

trench-parallel band between the coseismic slip patches and the up-dip zone of afterslip (Fig. 2). A less striking band of aftershocks northeast of Simeulue corresponds to the down-dip and southern edges of the Simeulue coseismic slip patch.

The temporal evolution of aftershocks may reflect a delayed response to the coseismic stress change of a population of small, volumetrically distributed, secondary faults (*42*). According to this model, the cumulative number of aftershocks should follow a $\log(1 + t/T_{as})$ evolution, mathematically equivalent to that of afterslip. However, we may expect different characteristic times, T_{as} and T_{GPS}, because each process should reflect independent responses to the coseismic stress change. An alternative mechanism has seismicity controlled by the stressing rate associated with afterslip (*44*). In this case, both processes should have the same characteristic time, as was found for aftershocks of the 1999 Chi-Chi, Taiwan, and 2001 Arequipa, Peru, earthquakes (*40*, *44*). A third potential model has aftershocks driven by the coseismic stress change but also includes the spatial and temporal modulation of stress-associated afterslip (*42*).

To test these models, we consider two near-field cGPS sites (LHWA and BSIM), which we compare to the temporal evolution of nearby aftershocks, and one far-field cGPS site (SAMP), which we compare to the deep aftershocks. We find a clear linear relationship between cumulative displacement and cumulative number of aftershocks in regions near these cGPS sites (Fig. 4, D to F). For SAMP, this linear relationship exists both after the 2004 M_w 9.1 event and after the 2005 event. The linear relationship between the cumulative number of aftershocks and the cumulative displacement at large times is not surprising (when presumably $t \gg T_{as}$ and $t \gg T_{GPS}$) because both processes should then vary linearly with the logarithm of time. The linear correlation in the early postseismic phase, when both aftershocks and afterslip depart from a linear dependence on the logarithm of time (Fig. 5 and fig. S9), is more meaningful. In the context of the functional form adopted here, the aftershocks and the afterslip have characteristic times that differ by no more than a factor of 2, although we cannot determine whether the times are exactly the same (Fig. 5). We note that a related observation for repeating earthquakes in the Loma Prieta aftershock zone suggests that the recurrence interval follows the characteristic inverse time decay, consistent with a model in which the repeating events are driven by creeping in the surrounding medium (*45*).

Our present models are limited by the lack of detailed structural information, in particular the role of splay and strike-slip faults and variations in elastic structure. Despite the limitations of the existing models, the 2005 Nias-Simeulue earthquake clearly illustrates the importance of aseismic slip on the shallowest portion of the megathrust. A wide variety of interseismic, coseismic, and postseismic data from the northern Sumatran forearc suggests that frictional behavior of the megathrust varies abruptly in space but not rapidly in time. Early near-field deformation following the 2005 Nias-Simeulue earthquake is dominated by afterslip on the megathrust, and both afterslip and aftershocks have the same functional dependence on time. Although temperature might be a key factor controlling regional upper and lower limits to seismogenic patches and down-dip variations of frictional properties, other factors must be called upon to explain the long-lived along-strike variations of the mode of slip seen here and in other subduction zones (*12*, *13*).

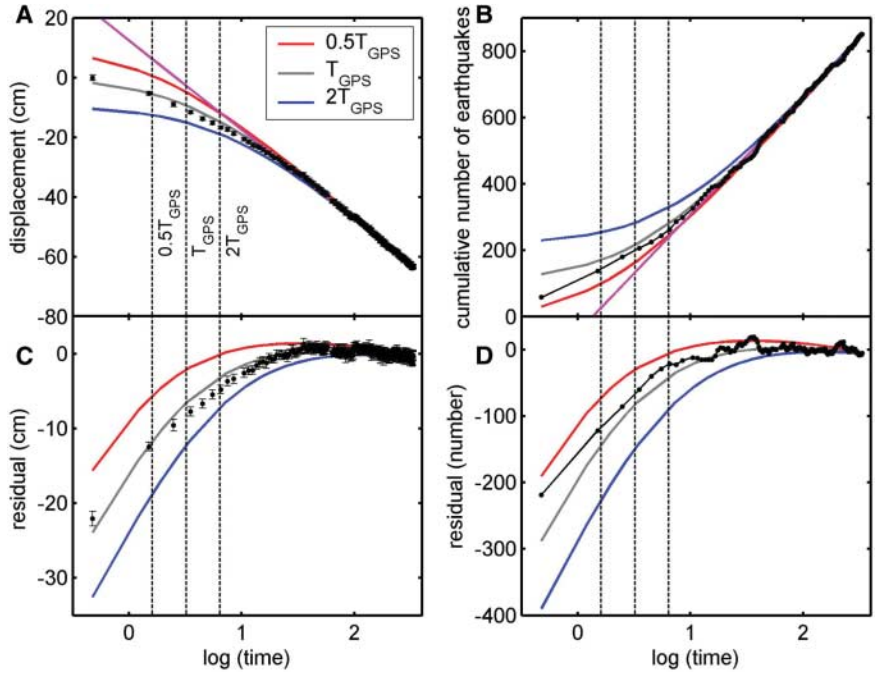

Fig. 5. (**A**) Comparison between the north component of postseismic displacement at LHWA (black dots, same as Fig. 4A) and modeled displacements [(*23*), eq. S1]. The gray line corresponds to the best-fit parameter values and is the same as in Fig. 4A, but in linear-log space. The blue and red lines correspond to fixing the estimates of T_{GPS} to be a factor of 2 greater and less than the optimal values, respectively. Pink lines denote roughly linear variations of postseismic displacement with the logarithm of time when $t \gg T_{GPS}$ [(*23*), eq. S4]. (**B**) Same as (A) but for cumulative number of aftershocks. We fix T_{as} to be the same as T_{GPS} and only invert for the amplitude [(*23*), eq. S6]. (**C** and **D**) Residuals between model curves and observations with respect to the pink line. The temporal evolutions of afterslip and aftershock are bounded by model curves with characteristic time between $0.5T_{GPS}$ and T_{GPS}.

References and Notes

1. S. E. Barrientos, G. Plafker, E. Lorca, *Geophys. Res. Lett.* **19**, 701 (1992).
2. S. C. Cohen, *Adv. Geophys.* **41**, 134 (1999).
3. C. Zweck, J. T. Freymueller, S. C. Cohen, *J. Geophys. Res.* **107**, 10.1029/2001JB000409 (2002).
4. J. F. Pacheco, L. R. Sykes, C. H. Scholz, *J. Geophys. Res.* **98**, 14133 (1993).
5. C. H. Scholz, *Nature* **391**, 37 (1998).
6. R. D. Hyndman, M. Yamano, D. A. Oleskevich, *Island Arc* **6**, 244 (1997).
7. D. A. Oleskevich, R. D. Hyndman, K. Wang, *J. Geophys. Res.* **104**, 14965 (1999).
8. S. M. Peacock, R. D. Hyndman, *Geophys. Res. Lett.* **26**, 2517 (1999).
9. T.-R. A. Song, M. Simons, *Science* **301**, 630 (2003).
10. R. E. Wells, R. J. Blakely, Y. Sugiyama, D. W. Scholl, P. A. Dinterman, *J. Geophys. Res.* **108**, 10.1029/2002JB002072 (2003).
11. Y. Yamanaka, M. Kikuchi, *J. Geophys. Res.* **109**, 10.1029/2003JB002683 (2004).
12. M. E. Pritchard, M. Simons, *J. Geophys. Res.*, in press.
13. S. Miyazaki, P. Segall, J. Fukuda, T. Kato, *Geophys. Res. Lett.* **31**, 10.1029/2003GL019410 (2004).
14. T. Lay *et al.*, *Science* **308**, 1127 (2005).
15. C. Subarya *et al.*, *Nature* **440**, 46 (2006).
16. Y. Bock *et al.*, *J. Geophys. Res.* **108**, 10.1029/2001JB000324 (2003).
17. K. Sieh, D. Natawidjaja, *J. Geophys. Res.* **105**, 28295 (2000).
18. J. F. Genrich *et al.*, *J. Geophys. Res.* **105**, 28327 (2000).
19. D. H. Natawidjaja *et al.*, *J. Geophys. Res.* **109**, B04306 (2004).
20. K. R. Newcomb, W. R. McCann, *J. Geophys. Res.* **92**, 421 (1987).
21. Data are available at the Sumatran Plate Boundary Project site (www.tectonics.caltech.edu/sumatra).
22. K. Sieh, S. N. Ward, D. Natawidjaja, B. W. Suwargadi, *Geophys. Res. Lett.* **26**, 3141 (1999).
23. See supporting material on *Science* Online.
24. R. W. Briggs *et al.*, *Science* **311**, 1897 (2006).
25. E. R. Engdahl, A. Villasenor, H. R. DeShon, *Bull. Seismol. Soc. Am.*, in press.
26. O. Konca *et al.*, *Bull. Seismol. Soc. Am.*, in press.
27. J. J. McGuire, P. Segall, *Geophys. J. Int.* **155**, 778 (2003).
28. P. Segall, M. Matthews, *J. Geophys. Res.* **102**, 22391 (1997).
29. The fit of the model to the GPS time series is not ideal for a short period immediately after the main shock (fig. S4) because the ENIF underestimates the surface displacements.
30. L. Prawirodirdjo *et al.*, *Geophys. Res. Lett.* **24**, 2601 (1997).
31. M. Simoes, J. P. Avouac, R. Cattin, P. Henry, *J. Geophys. Res.* **109**, 10.1029/2003JB002958 (2004).
32. T. J. Fitch, *J. Geophys. Res.* **77**, 4432 (1972).
33. R. McCaffrey, *Geology* **19**, 881 (1991).

34. D. E. Karig, M. B. Lawrence, G. F. Moore, J. R. Curray, *J. Geol. Soc. (London)* **137**, 77 (1980).
35. D. Natawidjaja, thesis, California Institute of Technology (2003).
36. H. Perfettini, J. P. Avouac, *J. Geophys. Res.* **109**, 10.1029/2003JB002917 (2004).
37. J. H. Dieterich, *J. Geophys. Res.* **84**, 2161 (1979).
38. A. Ruina, *J. Geophys. Res.* **88**, 359 (1983).
39. S. Miyazaki *et al.*, *Geophys. Res. Lett.* **31**, 10.1029/2004GL021457 (2004).
40. H. Perfettini, J. P. Avouac, J. C. Ruegg, *J. Geophys. Res.* **110**, 10.1029/2004JB003522 (2005).
41. M. L. Blanpied, D. A. Lockner, J. D. Byerlee, *J. Geophys. Res.* **100**, 13045 (1995).
42. J. Dieterich, *J. Geophys. Res.* **99**, 2601 (1994).
43. Seismicity obtained from Incorporated Research Institutions for Seismology (IRIS) (www.iris.washington.edu/SeismiQuery/events.htm).
44. H. Perfettini, J. P. Avouac, *J. Geophys. Res.* **109**, 10.1029/2003JB002488 (2004).
45. D. P. Schaff, G. C. Beroza, B. E. Shaw, *Geophys. Res. Lett.* **25**, 4549 (1998).
46. M. Chlieh *et al.*, paper presented at the American Geophysical Union fall meeting, San Francisco, 5 to 9 December 2005, abstract A05j.
47. Supported by the Gordon and Betty Moore Foundation and the Indonesian International Joint Research Program (RUTI). We thank two anonymous reviewers for constructive comments, as well as R. W. Briggs, H. Perfettini, and A. J. Meltzner for valuable discussions. This is Caltech Tectonics Observatory contribution number 40 and Caltech Seismological Laboratory contribution number 9146.

Supporting Online Material

www.sciencemag.org/cgi/content/full/312/5782/1921/DC1
Materials and Methods
Figs. S1 to S10
References

2 March 2006; accepted 17 May 2006
10.1126/science.1126960

REPORTS

Spin-Wave Lifetimes Throughout the Brillouin Zone

S. P. Bayrakci,[1]* T. Keller,[1,2] K. Habicht,[3] B. Keimer[1]

We used a neutron spin-echo method with microelectron-volt resolution to determine the lifetimes of spin waves in the prototypical antiferromagnet MnF_2 over the entire Brillouin zone. A theory based on the interaction of spin waves (magnons) with longitudinal spin fluctuations provides an excellent, parameter-free description of the data, except at the lowest momenta and temperatures. This is surprising, given the prominence of alternative theories based on magnon-magnon interactions in the literature. The results and technique open up a new avenue for the investigation of fundamental concepts in magnetism. The technique also allows measurement of the lifetimes of other elementary excitations, such as lattice vibrations, throughout the Brillouin zone.

The concept of elementary excitations is one of the basic pillars of the theory of solids. In the low-temperature, long-wavelength limit, such excitations do not interact and have an infinite lifetime. For nonzero temperatures and momenta, the lifetimes of elementary excitations are generally limited by collisions with other excitations, with important consequences for the macroscopic properties of solids. For instance, the thermal expansion of solids can be understood as a consequence of collisions between lattice vibrations (phonons). Because of their comparatively simple Hamiltonians, magnetically ordered states are excellent testing grounds for theories of elementary excitations and their interactions. Nevertheless, the damping of spin waves in antiferromagnets has remained an open problem for four decades. Theoretical calculations of magnon lifetimes have been carried out since the 1960s, with intensive development occurring on several fronts in the early 1970s. However, these activities ground to a halt by the mid-1970s due to the lack of appropriate experimental data, namely, from momentum-resolved measurements with sufficient energy resolution. The only low-temperature data available were taken with momentum $q \cong 0$, in antiferromagnetic resonance (AFMR) and parallel pumping measurements (*1*, *2*). Because of the limited energy resolution, momentum-resolved data from neutron spectroscopy (*3*), by contrast, were confined to the critical regime extremely close to the Néel temperature (T_N), where most theories do not apply. Until recently, no other experimental techniques were available that permitted high-resolution measurements of excitation lifetimes at low temperatures over the whole Brillouin zone. We report on a neutron spectroscopy method with μeV resolution that is used to measure spin-wave (magnon) lifetimes in the prototypical antiferromagnet MnF_2 over the temperature range 0.04 to 0.6 T_N. The results subject long-standing theoretical predictions to a first experimental test and hold promise as a probe of elementary excitations in quantum

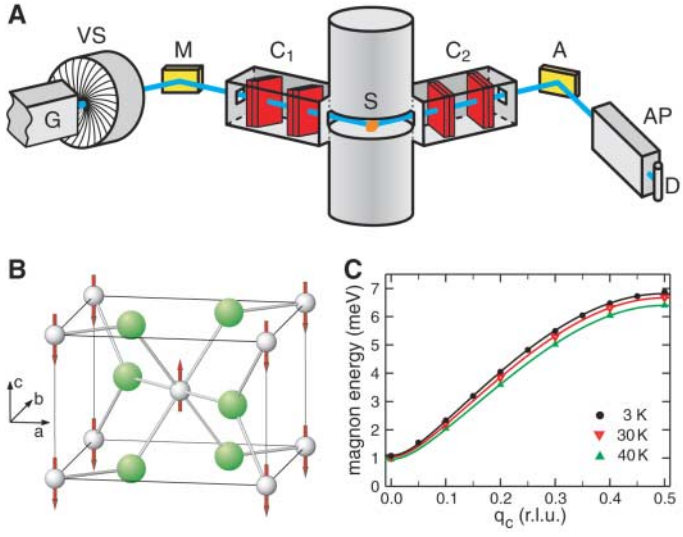

Fig. 1. (**A**) A diagram of the spectrometer TRISP at the FRM-II. G denotes the polarizing guide and AP the transmission polarizer; M and A are the monochromator and analyzer, as in TAS. S is the sample and D the detector; VS indicates the velocity selector. The resonance coil pairs (C_1 and C_2) are shown in red, and the mu-metal shielding boxes that enclose them in gray. The blue ray represents the path of the neutrons through the spectrometer, from left to right in the diagram. (**B**) The crystal and magnetic structure of MnF_2. The gray (smaller) spheres represent Mn^{2+} ions and the green (larger) spheres the F^- ions. The arrows indicate the relative directions of the Mn^{2+} spins on the respective sublattices. (**C**) The magnon dispersion along the q_c direction at three selected temperatures at and below 40 K. The data were taken on TRISP during the course of the linewidth measurements. The curves show the results of fits based on the same spin-wave result used by Okazaki *et al.* (*8*), in which the anisotropy is expressed by a single-ion form and the interactions of up to third-nearest neighbors are taken into account.

[1]Max-Planck-Institut für Festkörperforschung, Heisenbergstrasse 1, 70569 Stuttgart, Germany. [2]Forschungsreaktor München II, Zentrale Wissenschaftliche Einrichtung der Technischen Universität München (ZWE FRM II), Lichtenbergstrasse 1, 85748 Garching, Germany. [3]Hahn-Meitner-Institut, Glienickerstrasse 100, 14109 Berlin, Germany.

*To whom correspondence should be addressed. E-mail: bayrakci@fkf.mpg.de